International Journal of Fracture (2006) 139:91–117
DOI 10.1007/s10704-006-0024-4

J resistance behavior in functionally graded materials using cohesive zone and modified boundary layer models

DO-JUN SHIM, GLAUCIO H. PAULINO* and ROBERT H. DODDS Jr
Department of Civil & Environmental Engineering, University of Illinois at Urbana-Champaign, Newmark Laboratory, 205 North Mathews Avenue, Urbana, IL 61801, USA
**Author for correspondence (E-mail: paulino@uiuc.edu)*

Received 30 September 2005; accepted 26 January 2006

Abstract. This paper describes elastic–plastic crack growth resistance simulation in a ceramic/metal functionally graded material (FGM) under mode I loading conditions using cohesive zone and modified boundary layer (MBL) models. For this purpose, we first explore the applicability of two existing, phenomenological cohesive zone models for FGMs. Based on these investigations, we propose a new cohesive zone model. Then, we perform crack growth simulations for TiB/Ti FGM SE(B) and SE(T) specimens using the three cohesive zone models mentioned above. The crack growth resistance of the FGM is characterized by the J-integral. These results show that the two existing cohesive zone models overestimate the actual J value, whereas the model proposed in the present study closely captures the actual fracture and crack growth behaviors of the FGM. Finally, the cohesive zone models are employed in conjunction with the MBL model. The two existing cohesive zone models fail to produce the desired K–T stress field for the MBL model. On the other hand, the proposed cohesive zone model yields the desired K–T stress field for the MBL model, and thus yields J_R curves that match the ones obtained from the SE(B) and SE(T) specimens. These results verify the application of the MBL model to simulate crack growth resistance in FGMs.

Key words: 3-D finite element analysis, cohesive zone model, crack growth resistance curve, elastic–plastic crack growth, functionally graded material (FGM), J-integral, modified boundary layer model.

1. Introduction

Functionally graded materials (FGMs) are new advanced multifunctional materials, which are tailored to take advantage of its constituents, e,g. in a ceramic/metal FGM, heat and corrosion resistance of ceramics together with mechanical strength and toughness of metals. To keep pace with application and performance demands of FGMs, scientific knowledge of fracture and damage tolerance is important for improving their structural integrity. Fracture characteristics of FGMs have been investigated by many researchers during the past years, e.g. Eischen (1987), Erdogan (1995), Gu and Asaro (1997), Anlas et al. (2000), Kim and Paulino (2002a, 2003), and Walters (2004, 2005, 2006). In the present study, fracture behaviors of FGMs are investigated with special emphasis on the crack growth resistance using cohesive zone and modified boundary layer (MBL) models. Experimental results reported by Li et al. (2000), Abanto-Bueno and Lambros (2002), Moon et al. (2002), and Tohgo et al. (2005) demonstrate that the crack growth resistance curves for

FGMs follow the crack-bridging concept for the materials investigated, which suggest that a cohesive zone model can be used to simulate crack growth resistance in FGMs.

Needleman (1987) pioneered the computational scheme of interface-cohesive surfaces to nucleate and propagate cracks in finite element (FE) models. This work lead to the introduction of the exponential form for the traction–displacement relationship (Needleman, 1990). Sebsequent researchers employed this and other types of traction–displacement relationships to investigate various issues, e.g. void nucleation (Tvergaard, 1990), quasi-static crack growth (Tvergaard and Hutchinson, 1992), crack growth in ductile materials (Roy and Dodds, 2001; Tvergaard, 2001), dynamic crack growth and impact damage in brittle materials (Xu and Needleman, 1996; Camacho and Ortiz, 1996; Siegmund and Needleman, 1997; Geubelle and Baylor, 1998; Zavattieri and Espinosa, 200l; Zhang and Paulino, 2005).

While cohesive zone modeling for homogeneous materials has been widely investigated, its application to FGMs is still limited due to the complex, graded microstructures within these materials. Jin et al. (2002) proposed a volume fraction-based, phenomenological cohesive zone model for FGMs and later employed this model to simulate elastic–plastic crack growth in TiB/Ti FGMs (Jin et al., 2003). Tvergaard (2002) addressed theoretical issues related to the application of cohesive zone model to study crack growth in FGMs. Rangaraj and Kokini (2004) studied thermal fracture behaviors in functionally graded thermal barrier coatings using cohesive zone modeling. Jin and Dodds (2004) studied crack growth resistance behaviors in ceramic/metal FGMs. Zhang and Paulino (2005) and Kandula et al. (2005) presented cohesive zone modeling of dynamic fracture in FGMs.

Recently, Shim et al. (2006a) developed a MBL model for FGMs. In their study, they demonstrated the applicability of the MBL model to analyze various fracture problems in FGMs. The motivation of the present study is to employ the MBL model to investigate crack growth resistance behaviors in ceramic/metal FGMs. For this purpose, we first explore the applicability of existing cohesive zone models for FGMs. Based on these investigations, we propose a new cohesive zone model. Then, we perform crack growth simulations for TiB/Ti FGM SE(B) and SE(T) specimens using the three cohesive zone models. The crack growth resistance of the FGM is characterized by the path independent J-integral. These results are investigated to evaluate the relevance of the three cohesive zone models. Finally, the cohesive zone models are employed in conjunction with the MBL model. The crack growth resistance curves obtained from the MBL model are compared with those obtained from the fracture specimens to verify the applicability of the MBL model.

The remainder of the paper is organized as follows. Section 2 describes the two existing cohesive zone models for FGMs and also presents a new cohesive zone model. Section 3 describes the three-dimensional (3-D) finite element formulation with graded solid and interface-cohesive elements tailored for application to FGMs. Section 4 presents the crack growth resistance behavior of TiB/Ti FGM SE(B) and SE(T) specimens. Section 5 describes the application of cohesive zone modeling to the MBL model. Finally, Section 6 provides some concluding remarks.

2. On cohesive zone models for FGMs

While the cohesive zone approach has proven a convenient and effective method to simulate and analyze crack growth in homogeneous materials, generalization of the cohesive zone concept to model fracture in FGMs involves a challenging task due to the complicated microstructures and the related failure mechanisms in FGMs. Jin et al. (2002) proposed a volume fraction-based, phenomenological cohesive zone model for FGMs, which introduces two material-specific parameters that account for the interaction between different material phases. Recently, Zhang and Paulino (2005) adopted the bilinear cohesive zone model to the volume fraction-based, phenomenological cohesive zone model to simulate dynamic failure in FGMs. This section first reviews and discusses the phenomenological cohesive zone models proposed by Jin et al. (2002) and Zhang and Paulino (2005). Then, based on these discussions, a new volume fraction-based, phenomenological cohesive zone model is proposed for simulating crack growth in FGMs.

In the present study, we only consider crack growth under mode I conditions, where the crack is parallel to the material gradient. The description thus adopts a tensile mode formulation. Crack growth in FGMs under mixed-mode conditions was recently addressed by Kim and Paulino (2004), however, they did not employ a cohesive zone approach. Figure 1 shows a schematic representation of the cohesive zone concept and the cohesive tractions acting along the cohesive surface under mode I conditions. Here, δ and σ denote the normal displacement jump across the cohesive surface and the corresponding normal cohesive traction, respectively.

2.1. Exponential cohesive zone model

Jin et al. (2002) assumed a cohesive energy potential of the cohesive zone in a ceramic/metal FGM in the following volume fraction-based form

$$\phi(\bar{x}, \delta, \kappa) = \frac{V_{\text{met}}(\bar{x})}{V_{\text{met}}(\bar{x}) + \beta_{\text{met}}[1 - V_{\text{met}}(\bar{x})]}\phi_{\text{met}}(\delta, \kappa) + \frac{1 - V_{\text{met}}(\bar{x})}{1 - V_{\text{met}}(\bar{x}) + \beta_{\text{cer}} V_{\text{met}}(\bar{x})} \times \phi_{\text{cer}}(\delta, \kappa) \tag{1}$$

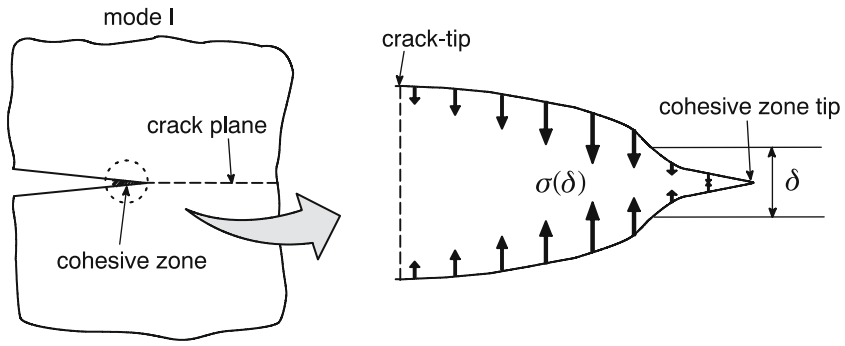

Figure 1. Schematic representation of the cohesive zone concept, showing cohesive tractions acting along the cohesive surface at crack-tip under mode I conditions.

with the effective cohesive traction given by

$$\sigma_{\text{eff}} = \frac{\partial \phi}{\partial \delta} = \frac{V_{\text{met}}(\bar{x})}{V_{\text{met}}(\bar{x}) + \beta_{\text{met}}[1 - V_{\text{met}}(\bar{x})]} \frac{\partial \phi_{\text{met}}}{\partial \delta} + \frac{1 - V_{\text{met}}(\bar{x})}{1 - V_{\text{met}}(\bar{x}) + \beta_{\text{cer}} V_{\text{met}}(\bar{x})} \frac{\partial \phi_{\text{cer}}}{\partial \delta}, \quad (2)$$

where $V_{\text{met}}(\bar{x})$ denotes the volume fraction of the metal, $\bar{x} = (x_1, x_2, x_3), \kappa$ is an internal variable which evolves according to a set of kinetic relations describing the irreversible processes of decohesion, β_{met} and β_{cer} are two cohesive gradation parameters that describe the transition of failure mechanisms from pure ceramic to pure metal. The parameters β_{met} and β_{cer} are material-dependent and are calibrated via experiments. Under loading conditions (described by κ), the cohesive energy potential for the metal and ceramic phases, ϕ_{met} and ϕ_{cer}, are selected as

$$\phi_{\text{met}} = \mathrm{e}\sigma_{\text{met}}^{\max} \delta_{\text{met}}^{\text{c}} \left[1 - \left(1 + \frac{\delta}{\delta_{\text{met}}^{\text{c}}} \right) \exp\left(-\frac{\delta}{\delta_{\text{met}}^{\text{c}}} \right) \right], \quad (3)$$

$$\phi_{\text{cer}} = \mathrm{e}\sigma_{\text{cer}}^{\max} \delta_{\text{cer}}^{\text{c}} \left[1 - \left(1 + \frac{\delta}{\delta_{\text{cer}}^{\text{c}}} \right) \exp\left(-\frac{\delta}{\delta_{\text{cer}}^{\text{c}}} \right) \right], \quad (4)$$

respectively. The cohesive tractions of the metal and ceramic phases thus follow (e.g., Xu and Needleman, 1996; Siegmund and Needleman, 1997; Ortiz and Pandolfi, 1999; Roy and Dodds, 2001)

$$\sigma_{\text{met}} = \frac{\partial \phi_{\text{met}}}{\partial \delta} = \mathrm{e}\sigma_{\text{met}}^{\max} \left(\frac{\delta}{\delta_{\text{met}}^{\text{c}}} \right) \exp\left(-\frac{\delta}{\delta_{\text{met}}^{\text{c}}} \right), \quad (5)$$

$$\sigma_{\text{cer}} = \frac{\partial \phi_{\text{cer}}}{\partial \delta} = \mathrm{e}\sigma_{\text{cer}}^{\max} \left(\frac{\delta}{\delta_{\text{cer}}^{\text{c}}} \right) \exp\left(-\frac{\delta}{\delta_{\text{cer}}^{\text{c}}} \right), \quad (6)$$

where $\mathrm{e} = \exp(1)$, $\sigma_{\text{met}}^{\max}$ is the maximum cohesive traction of the metal phase, $\delta_{\text{met}}^{\text{c}}$ is the value of δ at $\sigma = \sigma_{\text{met}}^{\max}$, $\sigma_{\text{cer}}^{\max}$ is the maximum cohesive traction of the ceramic phase, and $\delta_{\text{cer}}^{\text{c}}$ is the value of δ at $\sigma = \sigma_{\text{cer}}^{\max}$. This model adopts a computationally convenient, exponential form for the cohesive energy potentials for both metal and ceramic phases.

Substitution of Equations (3) and (4) into Equation (2) yields the effective cohesive traction for FGMs under loading conditions

$$\begin{aligned} \sigma_{\text{eff}} = {} & \frac{V_{\text{met}}(\bar{x})}{V_{\text{met}}(\bar{x}) + \beta_{\text{met}}[1 - V_{\text{met}}(\bar{x})]} \mathrm{e}\sigma_{\text{met}}^{\max} \left(\frac{\delta}{\delta_{\text{met}}^{\text{c}}} \right) \exp\left(-\frac{\delta}{\delta_{\text{met}}^{\text{c}}} \right) \\ & + \frac{1 - V_{\text{met}}(\bar{x})}{1 - V_{\text{met}}(\bar{x}) + \beta_{\text{cer}} V_{\text{met}}(\bar{x})} \mathrm{e}\sigma_{\text{cer}}^{\max} \left(\frac{\delta}{\delta_{\text{cer}}^{\text{c}}} \right) \exp\left(-\frac{\delta}{\delta_{\text{cer}}^{\text{c}}} \right), \quad \text{if } \delta = \delta_{\max} \text{ and } \dot{\delta} \geq 0. \end{aligned} \quad (7)$$

For the unloading case, the model assumes

$$\sigma_{\text{eff}} = \left(\frac{\sigma_{\max}}{\delta_{\max}} \right) \delta, \quad \text{if } \delta < \delta_{\max} \quad \text{or } \dot{\delta} < 0, \quad (8)$$

where $\sigma_{\max}$ is the value of σ at $\delta = \delta_{\max}$ calculated from Equation (7).

The effective cohesive energy density, or the work of separation per unit area of cohesive surface, is defined by

$$\Gamma_{\text{eff}}^{\text{c}} = \int_0^{\infty} \sigma_{\text{eff}}(\delta)\, \mathrm{d}\delta. \tag{9}$$

Substituting Equation (7) into the above equation yields

$$\Gamma_{\text{eff}}^{\text{c}}(\bar{x}) = \frac{V_{\text{met}}(\bar{x})}{V_{\text{met}}(\bar{x}) + \beta_{\text{met}}[1 - V_{\text{met}}(\bar{x})]}\Gamma_{\text{met}}^{\text{c}} + \frac{1 - V_{\text{met}}(\bar{x})}{1 - V_{\text{met}}(\bar{x}) + \beta_{\text{cer}} V_{\text{met}}(\bar{x})}\Gamma_{\text{cer}}^{\text{c}}, \tag{10}$$

where $\Gamma_{\text{met}}^{\text{c}}$ and $\Gamma_{\text{cer}}^{\text{c}}$ denote the cohesive energy densities of the metal and ceramic phases, respectively:

$$\Gamma_{\text{met}}^{\text{c}} = \mathrm{e}\sigma_{\text{met}}^{\max}\delta_{\text{met}}^{\text{c}}, \qquad \Gamma_{\text{cer}}^{\text{c}} = \mathrm{e}\sigma_{\text{cer}}^{\max}\delta_{\text{cer}}^{\text{c}}. \tag{11}$$

Equation (10) shows that the cohesive energy density follows the same rule as that of the cohesive traction. Figure 2 shows a typical shape of the traction–displacement curve for the exponential cohesive zone model.

In the previous work by Jin et al. (2003) and by Jin and Dodds (2004), the above cohesive zone model was used to investigate crack growth resistance in TiB/Ti FGMs. They assume that the metal phase (Ti) controls the crack growth, and thus the extinction of cohesive elements is based on the critical displacement of the metal phase $\delta_{\text{met}}^{\text{c}}$ (see Section 3 for more detail).

Insertion of *intrinsic* cohesive elements introduces an artificial compliance to the structure (e.g., Baylor, 1998; Klein et al., 2000; Zhang, 2003). The magnitude of the artificial compliance is primarily related to the initial slope of the

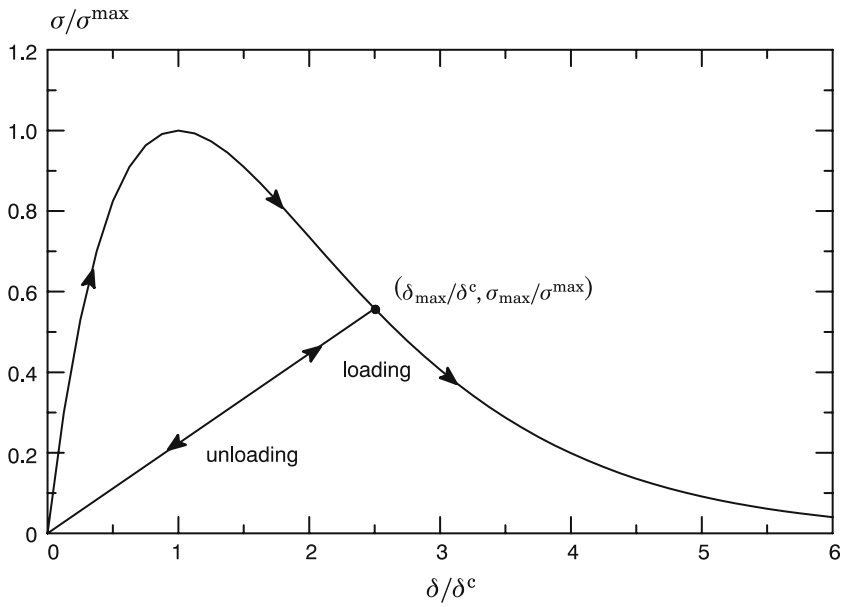

Figure 2. Typical traction–displacement curve for exponential cohesive zone model, where traction and displacement are normalized by maximum traction and critical displacement, respectively.

traction–displacement curve. For the exponential cohesive zone model, the traction–displacement curve has a defined shape, and thus defined initial slope. When the crack trajectory is known a priori, the effect of the artificial compliance may not be as significant for ductile materials – in general, the shape of the cohesive traction–displacement curve is not significant as the cohesive energy density and the maximum cohesive traction in simulating fracture in ductile materials (Tvergaard and Hutchinson, 1992). However, for relatively brittle materials, the introduction of the artificial compliance may have a significant effect on the numerical results. In the previous work by Jin and Dodds (2004), the effect of the artificial compliance to crack growth resistance in TiB/Ti FGM, which is a relatively brittle material, was not investigated.

2.2. Traction-based bilinear cohesive zone model

Bilinear cohesive zone models have been adopted for simulating impact damage in brittle materials (e.g., Zavattieri and Espinosa, 2001; Kandula et al., 2005). The bilinear cohesive zone model allows the user to control the initial slope of the traction–displacement curve, and thus restrict the effect of the artificial compliance (Geubelle and Baylor, 1998). The cohesive law for homogeneous material under mode I loading is stated as

$$\sigma = \sigma^{\max}\left(\frac{\delta^{c}-\delta^{*}}{\delta^{c}-\delta^{p}}\right)\frac{\delta}{\delta^{*}}, \tag{12}$$

where $\sigma^{\max}$ is the maximum cohesive traction, δ^{c} is the critical displacement, δ^{P} is the value of δ at $\sigma=\sigma^{\max}$ and δ^{*} is defined as

$$\begin{aligned} \delta^{*} &= \delta^{p}, \quad \text{if } \delta \leqq \delta^{p}, \\ &= \delta, \quad \text{if } \delta > \delta^{p}. \end{aligned} \tag{13}$$

The value of δ^{P} can be set close to zero to ensure initially stiff cohesive bond. The material fails when displacement δ reaches the critical displacement δ^{c}. Figure 3 shows the traction–displacement curve based on Equations (12) and (13).

In order to simulate brittle, dynamic crack growth in FGMs, Zhang and Paulino (2005) extended the above bilinear model to the volume fraction-based, phenomenological cohesive zone model described in Section 2.1. The effective cohesive traction for FGM is calculated by the volume fraction-based formula and traction associated with each material phase, which is determined from Equations (12) and (13) – the parameter δ^{p} is evaluated for each material phase. In the present study, we refer to this model as the *traction-based bilinear cohesive zone model*. The traction–displacement relationship for a ceramic/metal FGM under loading conditions can be expressed as

$$\begin{aligned} \sigma_{\text{eff}} = {} & \frac{V_{\text{met}}(\bar{x})}{V_{\text{met}}(\bar{x})+\beta_{\text{met}}[1-V_{\text{met}}(\bar{x})]}\sigma_{\text{met}}^{\max}\left(\frac{\delta_{\text{met}}^{c}-\delta_{\text{met}}^{*}}{\delta_{\text{met}}^{c}-\delta_{\text{met}}^{p}}\right)\frac{\delta}{\delta_{\text{met}}^{*}} \\ & + \frac{1-V_{\text{met}}(\bar{x})}{1-V_{\text{met}}(\bar{x})+\beta_{\text{cer}}V_{\text{met}}(\bar{x})}\sigma_{\text{cer}}^{\max}\left(\frac{\delta_{\text{cer}}^{c}-\delta_{\text{cer}}^{*}}{\delta_{\text{cer}}^{c}-\delta_{\text{cer}}^{p}}\right)\frac{\delta}{\delta_{\text{cer}}^{*}}, \end{aligned} \tag{14}$$

where $V_{\text{met}}(\bar{x})$, β_{met}, and β_{cer} follow the same definitions as in Section 2.1. The unloading process is similar to that of the exponential cohesive zone model.

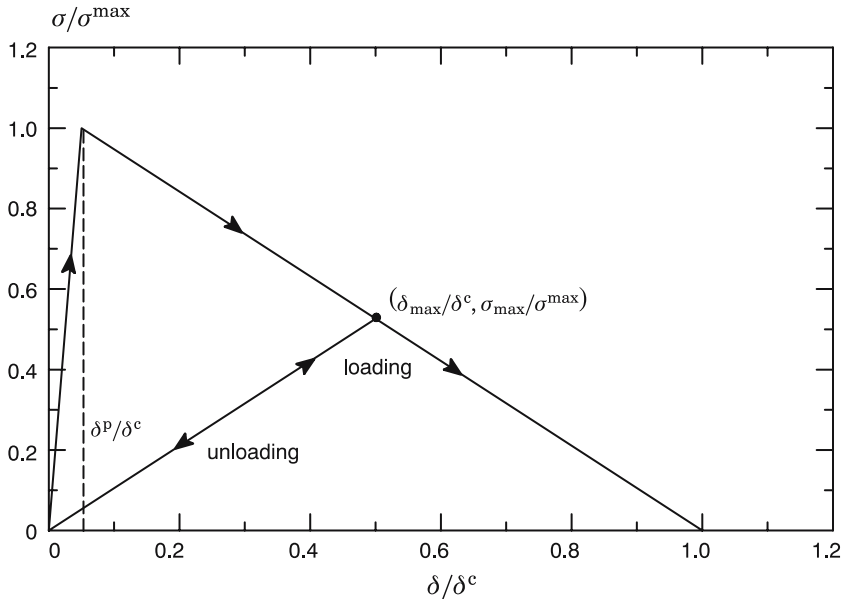

Figure 3. Typical traction–displacement curve for bilinear cohesive zone model, where traction and displacement are normalized by maximum traction and critical displacement, respectively.

The effective cohesive energy density Γ^c_{eff} for the bilinear cohesive model can also be defined by Equation (10). The cohesive energy densities of the metal and ceramic phases are given by

$$\Gamma^c_{met} = \frac{1}{2}\sigma^{max}_{met}\delta^c_{met}, \qquad \Gamma^c_{cer} = \frac{1}{2}\sigma^{max}_{cer}\delta^c_{cer}. \tag{15}$$

In the present study, we employ the above model to simulate crack growth resistance in TiB/Ti FGM. By introducing a steep initial slope, i.e. by assigning δ^p_{met} and δ^p_{cer} close to (but not equal to) zero, the effect of the artificial compliance to crack growth resistance is reduced. The above model also assumes that the metal phase controls the crack growth, and thus the extinction of the cohesive elements is based on the critical displacement of the metal phase δ^c_{met} (see Section 3 for more detail).

2.3. Displacement-based bilinear cohesive zone model

The two cohesive zone models described above, i.e. exponential and traction-based bilinear models, assume that the metal phase controls the crack growth behavior of the FGM. Such assumption is due to the fact that the cohesive fracture energy of the ceramic phase is relatively small compared to that of the metal phase. However, results from previous work (Carpenter et al., 1999) indicate that the cohesive fracture energy of TiB/Ti FGM is relatively small even for regions with relatively high-volume fraction of Ti, e.g. the cohesive fracture energy for 85% Ti and 15% TiB FGM is only about 7% that of pure Ti. In this sense, the cohesive element extinction criterion based on δ^c_{met} may not be suitable for FGMs. For example, consider a TiB/Ti FGM with a very low (less than 1%) volume fraction of Ti. It is obvious that the TiB phase (more than 99%), rather than the Ti phase, will control the crack growth behavior of

this material. These observations suggest that a volume fraction-based element extinction criterion is needed for FGMs.

In the present study, a *displacement-based bilinear cohesive zone model* for FGMs is proposed. This model is also based on the volume fraction-based, phenomenological cohesive zone model described in Section 2.1. Instead of calculating the effective cohesive traction, an effective critical displacement δ^{c}_{eff} is calculated from the volume fraction-based formula as follows:

$$\delta^{c}_{eff}(\bar{x}) = \frac{V_{met}(\bar{x})}{V_{met}(\bar{x}) + \beta_{met}[1 - V_{met}(\bar{x})]}\delta^{c}_{met} + \frac{1 - V_{met}(\bar{x})}{1 - V_{met}(\bar{x}) + \beta_{cer} V_{met}(\bar{x})}\delta^{c}_{cer}, \tag{16}$$

where δ^{c}_{met} and δ^{c}_{cer} are the critical displacements (cohesive parameters from the bilinear model) of metal and ceramic, respectively. The effective cohesive energy density Γ^{c}_{eff} is calculated from Equations (10) and (15). Then, the effective maximum cohesive traction can be defined as

$$\sigma^{max}_{eff} = 2\frac{\Gamma^{c}_{eff}}{\delta^{c}_{eff}}. \tag{17}$$

By substituting the effective values of σ^{max}, δ^{c}, and δ^{P}, i.e. σ^{max}_{eff}, δ^{c}_{eff}, and δ^{p}_{eff} (this is a user defined value close to zero), respectively, to Equations (12) and (13), a displacement-based bilinear cohesive zone model can be obtained.

3. Finite element modeling of FGMs

This section describes the formulation of both the 3-D solid element and the interface-cohesive element with graded material properties. For the solid elements which model the bulk (background) FGM, the J_2 flow theory with isotropic hardening describes the material behavior and the volume fraction-based model proposed by Tamura et al. (1973) (so called TTO model) characterizes the material properties (Young's modulus, Poisson's ratio, yield stress, and power hardening exponent) within the element. For the interface-cohesive elements, which initially have zero thickness, the material behavior and properties follow the functionally graded cohesive law described in Section 2.

3.1. Graded solid and interface elements formulation

For FGMs, material properties depend on spatial positions even within an element. Kim and Paulino (2002a,b) presented a generalized isoparametric formulation (GIF) to calculate the material properties within an element. The present study uses the GIF for both solid and interface elements. For 3-D solid elements, elastic and plastic properties are interpolated using shape functions, i.e.

$$E = \sum_{i=1}^{m} N_i E_i, \qquad \nu = \sum_{i=1}^{m} N_i \nu_i, \qquad \sigma_Y = \sum_{i=1}^{m} N_i \sigma_{Y_i}, \qquad n = \sum_{i=1}^{m} N_i n_i, \tag{18}$$

where $N_i (i = 1, 2, \ldots, m)$ are the standard finite element shape functions and m is the number of nodes in an element. Moreover, E_i, ν_i, σ_{Y_i}, and $n_i (i = 1, 2, \ldots, m)$ are the values of Young's modulus, Poisson's ratio, yield stress, and power hardening exponent at the nodal points, respectively. For the interface-cohesive element, we

only need to specify the metal volume fraction V_{met}, which is also calculated by the standard interpolation

$$V_{\text{met}} = \sum_{i=1}^{4} N_i V_{\text{met}}^i, \tag{19}$$

where $V_{\text{met}}^i (i = 1, 2, 3, 4)$ are the values of V_{met} at the nodal points of the interface-cohesive elements.

3.2. Finite element analysis technique

The numerical analyses based on small-displacement formulation are performed using WARP3D (Gullerud et al., 2004), a research finite element code for nonlinear fracture mechanics, which employs an incremental-iterative, implicit formulation. In addition to the conventional solid and interface-cohesive elements for homogeneous materials, this code also supports solid elements with graded elastic and plastic properties and interface-cohesive elements with graded cohesive traction and cohesive energy density.

Large load increments often specified in implicit solution methods may create an "overshoot" problem with nonlinear cohesive zone model, i.e. some interface elements may miss the peak cohesive traction by passing from the pre-peak to post-peak side of the traction–displacement curve within a single increment. This introduces inaccurate stress and deformation fields, which do not follow the constitutive cohesive law. To avoid these effects, WARP3D adaptively controls the size of the global load increments to enforce the proper cohesive constitutive response.

3.3. Cohesive element extinction technique

For the exponential cohesive zone model, WARP3D removes the cohesive element from the model (thereby growing the crack) when the effective displacement of a cohesive element reaches $5\delta_{\text{met}}^{\text{c}}$. For the bilinear cohesive zone model, element extinction occurs when the cohesive traction reduces to zero, or equivalently, when the effective opening displacement reaches the critical displacement. As described in the previous section, the element extinction condition for the traction-based bilinear cohesive zone model is similar to the exponential cohesive zone model, i.e. the critical displacement of the metal phase controls the element extinction. On the other hand, the displacement-based bilinear cohesive zone model uses an element extinction criterion based on Equation (16), i.e. the element extinction occurs when the effective displacement reaches the effective critical displacement defined by Equation (16). All the other features of FGM modeling described in the present work have been implemented in WARP3D.

4. *J* resistance curve behavior of ceramic/metal FGMs

4.1. TiB/Ti fracture specimen geometries, materials, and FE models

In the present study, numerical analyses of elastic–plastic crack growth are performed for both SE(B) and SE(T) specimens made of TiB/Ti FGM containing an initially

sharp crack front. Figure 4 shows the geometry of the SE(B) specimen used in the present study. The SE(T) specimen has the same geometry but is loaded in the longitudinal direction. The company CERCOM Inc. developed the TiB/Ti FGM system in a layered structural form for potential armor applications (Nelson and Ezis, 1996). Table 1 summarizes the geometric parameters of the SE(B) specimen used in both the present and experimental studies reported by Carpenter et al. (1999). In the present numerical analyses of the specimens, the idealized FGM composition varies from 100% TiB at the cracked surface to 100% Ti at the uncracked surface – the actual material variation from processing is presented by Carpenter et al. (1999). Thus ideally, the volume fraction of Ti (V_{Ti}) varies from zero at the cracked surface to one at the uncracked surface. The volume fraction of Ti within the specimen is approximated by a simple power function, i.e.

$$V_{\mathrm{Ti}}(y) = (y/W)^p, \tag{20}$$

where the power exponent $p = 0.84$ for the actual material variation (Jin et al., 2002). Table 2 lists the material properties of TiB and Ti – data from Carpenter et al. (1999), Paulino et al. (2001), Jin et al. (2003). The elastic–plastic material properties within the TiB/Ti FGM specimens are estimated by the TTO model of Tamura et al. (1973) – (see Jin et al., 2003 and Jin and Dodds, 2004 for more details). In the present study, we adopt the same material-dependent parameter $q = 4.5$ GPa for TiB/Ti FGM as in the previous studies (e.g. Williamson et al., 1993; Giannakopoulos et al., 1995; Carpenter et al., 1999; Jin et al., 2003).

Jin et al. (2003) showed that no crack tunneling develops for the TiB/Ti FGM SE(B) specimen considered in the present study, i.e. crack extension at the surface and mid-plane almost show no difference. In this sense, the present study employs a plane–strain condition FE model. Figure 5(a) shows the 3-D FE mesh used in the present study. Symmetry conditions permit modeling of only half of the specimen. The mesh consists of eight-node isoparametric solid elements and eight-node interface-cohesive elements. The interface-cohesive elements are placed only over the initial uncracked ligament. In the region beyond the initial crack front (6 mm), interface-cohesive elements have uniform size of 0.1 mm. The mesh has two layers of elements in the thickness direction and all nodes in the model are constrained in the thickness direction to obtain plane–strain conditions. The FE model has 3,324 nodes and 2,036 elements.

The finite element code WARP3D calculates the J-integral using the domain integral technique, which can be employed for homogeneous materials as well as for FGMs (Walters et al., 2004). The J values are evaluated for the three domains shown in Figure 5(b). Note that the domains are sufficiently remote from the initial crack-tip, and thus the crack-tip remains well within the domains during crack growth,

Table 1. Geometric parameters of fracture specimens.

Specimen	L (mm)	W (mm)	B (mm)	a_0/W	R (mm)
SE(B)	79.4	14.7	7.4	0.3	10.2
SE(T)	79.4	14.7	7.4	0.3	

Table 2. Material properties of Ti and TiB.

Material	Young's modulus (GPa)	Poisson's ratio	Yield stress (MPa)	Hardening exponent	Critical J_{Ic} (kJ/m^2)
Ti	107	0.34	450	14	24[a]
TiB	375	0.14	–	–	0.11

[a] Estimated from the experimental crack initiation load (Jin et al., 2003).

Figure 5(c). Moreover, only the solid elements within the domain contribute to the J evaluation. Numerical results show that the J values obtained from these domains match within 1% error throughout the crack growth analyses, verifying the path-independence of the J-integral. The J values presented in the following sections are obtained from the largest domain shown in Figure 5(b).

4.2. Determination of cohesive parameters

The uncoupled contribution of the metal and ceramic to the effective traction, Equations (7) and (14), or effective displacement, Equation (16), enables separate calibration of the cohesive parameters associated with metal and ceramic, respectively. The three cohesive zone models described in Section 2 have the following six material-dependent parameters that characterize the fracture process in a ceramic/metal FGM: Γ^{c}_{met} and Γ^{c}_{cer} (local work of separation of metal and ceramic, respectively), σ^{max}_{met} and σ^{max}_{cer} (maximum cohesive tractions of metal and ceramic, respectively), and, β_{met} and β_{cer} (cohesive gradation parameters). In addition to these six parameters, the bilinear cohesive zone model has two more parameter, i.e. δ^{p}_{met} and δ^{p}_{cer}, which are user defined values close to zero. In the present study, δ^{p}_{met} and δ^{p}_{cer} are defined as $\delta^{c}_{met}/100$ and $\delta^{c}_{cer}/100$, respectively, for both traction-based and displacement-based bilinear cohesive zone models.

Jin et al. (2003) discussed the details on the calibration procedure for the six cohesive parameters for the exponential cohesive zone model. They calibrated the cohesive parameters for a TiB/Ti FGM using experimental load versus crack extension responses for both Ti metal (Paulino et al., 2001) and TiB/Ti FGM SE(B) specimens

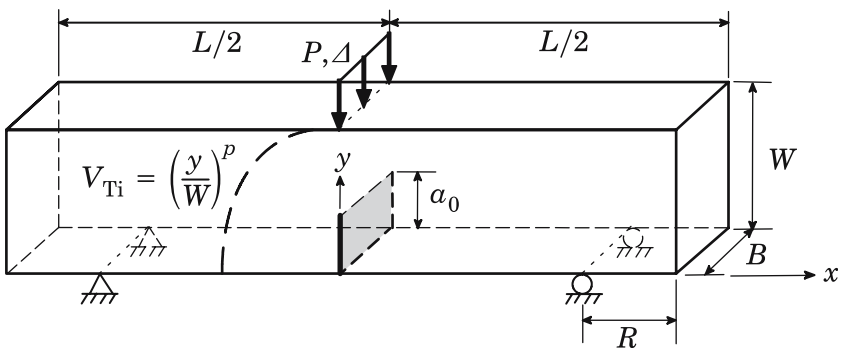

Figure 4. Geometry and material gradient of the SE(B) specimen.

Table 3. Calibrated cohesive parameters for TiB/Ti FGM.

Cohesive model	$\Gamma^{c}_{met}(=J^{met}_{Ic})$ (kJ/m^2)	$\sigma^{max}_{met}(=2.5\sigma_0)$ (MPa)	δ^{c}_{met} (mm)	β_{met}	$\Gamma^{c}_{cer}(=J^{cer}_{Ic})$ (kJ/m^2)	σ^{max}_{cer} (MPa)	δ^{c}_{cer} (mm)	β_{cer}
Exponential	24	1,125	0.008	18.5	0.11	22	0.0018	1.0
Traction bilinear	24	1,125	0.043	18.25	0.11	22	0.01	1.0
Disp. bilinear	24	1,125	0.043	50	0.11	22	0.01	1.0

(Carpenter et al., 1999). Based on these results, the parameters are calibrated for the bilinear cohesive zone models in the present study. Table 3 lists the calibrated cohesive parameters for the three cohesive zone models considered in the present study. In Table 3, σ_0 denotes the yield stress of the metal (Ti), and J^{met}_{Ic} and J^{cer}_{Ic} are the critical J-integrals at crack initiation for the metal and the ceramic (TiB), respectively. Note that β_{cer} is set to unity for all the cohesive zone models and β_{met} is calibrated by matching the experimental crack initiation load (Carpenter et al., 1999) with the numerical results.

Figure 6 compares the traction–displacement curves obtained from the three cohesive zone models using the parameters listed in Table 3 – here $V_{Ti} = 0.364$, which corresponds to the volume fraction of metal (Ti) at the initial crack-tip of the FGM specimen considered in the present study. Since the calibrated values of β_{met} are similar for the exponential model and the traction-based model (see Table 3), traction–displacement curves for the two models show similar trend – except that the traction-based bilinear model has a steeper initial slope. This is due to the fact that these two models assume that the metal phase controls the crack growth process. In Figure 6, the cohesive element extinction occurs for the exponential and the traction-based bilinear model when the effective displacement reaches 0.04 and 0.043 mm, respectively. On the other hand, for the displacement-based bilinear model, the cohesive element extinction occurs when the effective displacement reaches 0.007 mm, which is calculated from Equation (16). Also, the maximum effective traction for the displacement-based bilinear model is twice larger than that for the other two models. Moreover, the effective critical cohesive energy density, Γ^{c}_{eff}, for the displacement-based bilinear model is less than half of that for the other two models. Figure 7 compares the Γ^{c}_{eff} calculated from the three cohesive zone models (using parameters listed in Table 3) for the entire range of V_{Ti}. The Γ^{c}_{eff} calculated from the displacement-based bilinear model is smaller than that of the other two models for the entire range of V_{Ti}. Furthermore, the J_{Ic} values reported by Carpenter et al. (1999) for two specific values of V_{Ti} are more closely estimated by the displacement-based bilinear model.

4.3. Crack growth resistance of TiB/Ti FGM specimens

Figure 8 shows the load versus crack growth responses of the SE(B) specimen (Figure 4) obtained from the numerical analyses using three different cohesive zone models. Since the cohesive parameters are calibrated by matching the numerically obtained crack initiation load to that of the experimental one (0.925 kN), the crack

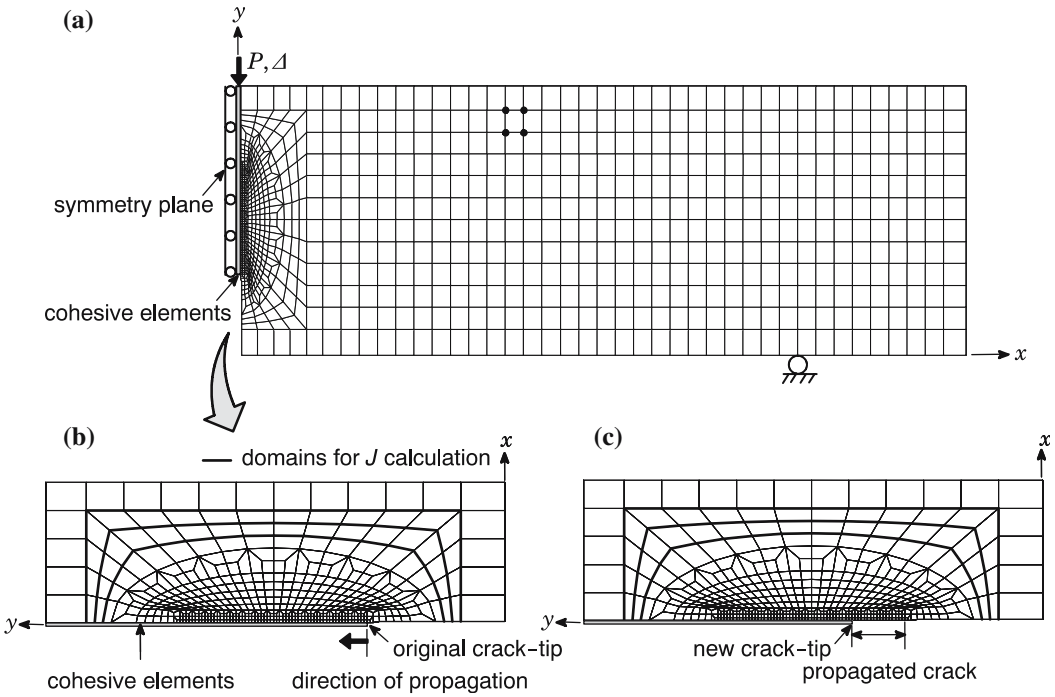

Figure 5. Longitudinal cross-section of the 3-D mesh used in the present study: (a) Overall view; (b) Close-up view of the crack-tip region showing the domains used for J calculation; (c) Crack growth via cohesive element extinction.

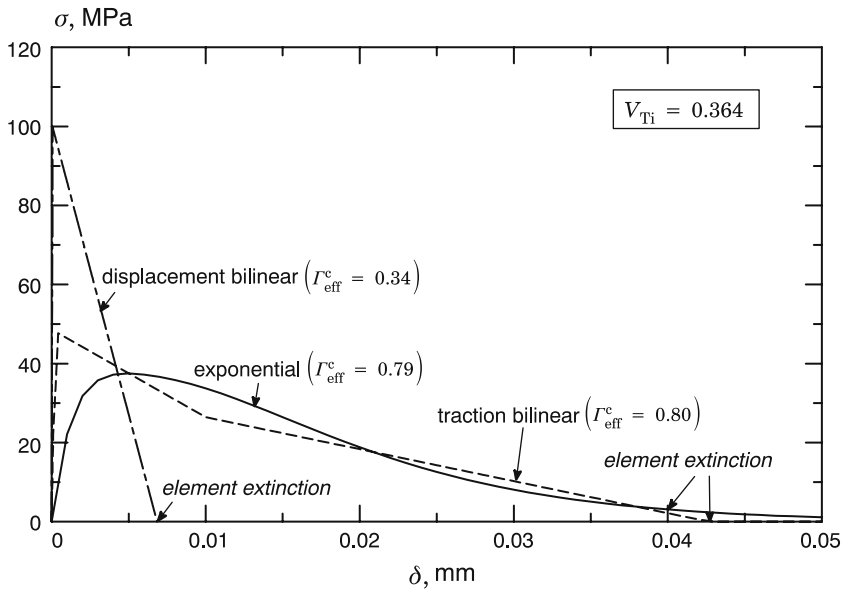

Figure 6. Traction–displacement curves obtained from the three cohesive zone models using the cohesive parameters listed in Table 3. Note that $V_{Ti} = 0.364$, which corresponds to the volume fraction of Ti at the initial crack-tip of the SE(B) specimen considered in the present study.

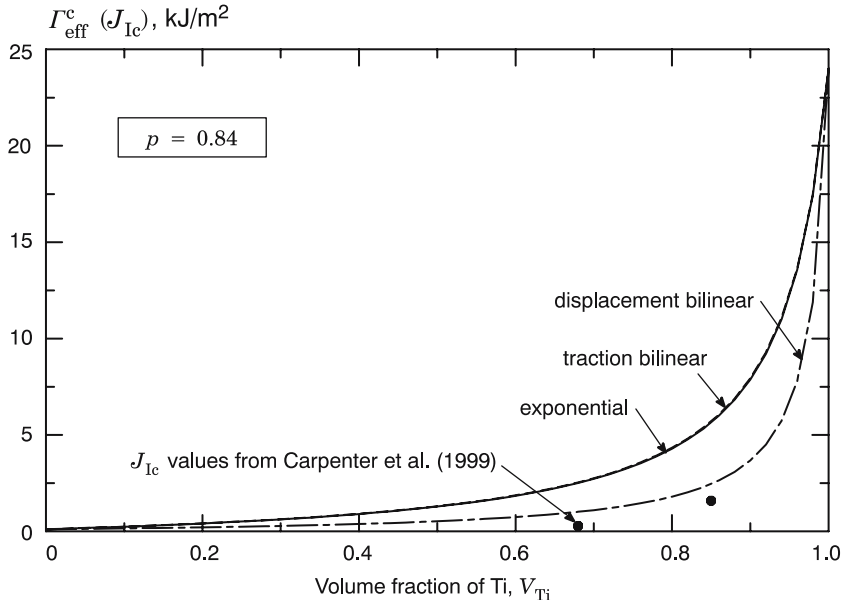

Figure 7. Effective critical cohesive energy densities calculated from the three cohesive zone models for the entire range of V_{Ti}. The J_{Ic} values for two specific values of V_{Ti} (Carpenter et al., 1999) are shown for comparison.

initiation loads from the three cohesive zone models approximately match each other in Figure 8. Note that, by matching the experimental crack initiation load, the three different cohesive zone models yield the same load versus crack growth response. Now, we compare the J resistance behavior of the SE(B) specimen obtained from these three models. Figure 9 shows the J-integral versus crack growth responses, i.e. J_R curves, obtained from the three cohesive zone models. Since the crack grows into a increasingly tough material, the J-integral increases with crack growth for all three models. However, the three cohesive zone models yield different J-integral values at crack initiation, J_{init}. The exponential and traction-based bilinear models show similar results, i.e. J_{init} values are near 2.0 kJ/m^2. On the other hand, J_{init} for the displacement-based bilinear model is about 0.5 kJ/m^2. Although the three cohesive models yield the same load versus crack growth response, the J-integral versus crack growth responses are quite different.

This phenomenon can be explained by observing the load versus crack mouth opening displacement (CMOD) and J-integral versus CMOD responses. Figure 10 shows the load versus CMOD curves obtained from the three cohesive zone models, as well as the curve obtained from a stationary crack model without cohesive elements. For the stationary crack model, the load increases almost linearly with the increasing CMOD in the range of loads considered, indicating little plastic deformation in the background material before crack initiation. Ideally, the result obtained from the cohesive zone model should match that of the stationary crack model before crack initiation. However, such result can only be obtained when an *extrinsic* cohesive zone model (e.g., Camacho and Ortiz, 1996; Ortiz and Pandolfi, 1999), is used. Since the cohesive zone models adopted in the present study are an *intrinsic* type, the artificial compliance introduced by the cohesive elements cause softening of the structure prior to crack initiation.

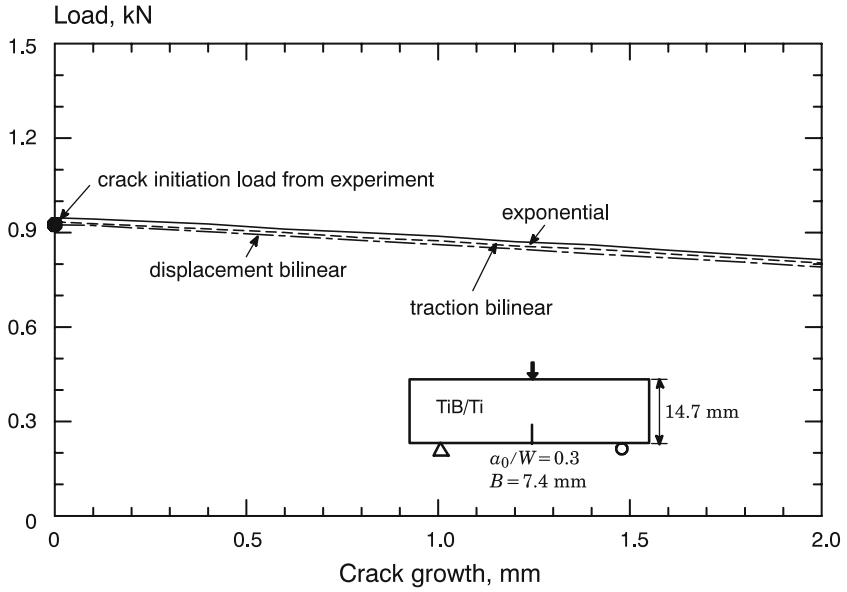

Figure 8. Load versus crack growth responses obtained from the three cohesive zone models for the TiB/Ti SE(B) specimen ($p = 0.84$).

The curve obtained from the exponential model shows large amount of softening, i.e. the initial slope of the curve in Figure 10 is much smaller than that of the stationary crack at the initial loading stage. The crack initiation occurs after the load passes the peak value. The CMOD at crack initiation for the exponential model is approximately seven times that of the stationary crack. This is due to the fact that the exponential model assumes that the metal phase (Ti) controls the crack growth. For the traction-based bilinear model (which has a steep initial slope, Figure 6), the initial slope of the load versus CMOD curve shown in Figure 10 is much larger than that of the exponential model, and is close to the initial slope of the stationary crack model. However, as the load increases, the curve obtained from the traction-based bilinear model deviates from the stationary crack curve and then closely follows the curve obtained from the exponential model beyond peak point. Since the traction-based bilinear model also assumes that the metal phase controls the crack growth, the value of CMOD at crack initiation is similar to that of the exponential model. For the displacement-based bilinear model, the initial slope of the curve is approximately same as that of the stationary crack model. Moreover, the two curves, i.e. displacement-based bilinear model and stationary crack model, show relatively good agreement up to the peak point, indicating small amount of softening effect. The crack initiation for the displacement-based bilinear model (which is based on the effective critical displacement) occurs just after the peak load and the corresponding CMOD value is approximately twice larger than that of the stationary crack, but is three times smaller than that of the other two models.

Figure 11 shows the J-integral versus CMOD curves obtained from the three cohesive zone models and the stationary crack model. Here again, ideally, the curve obtained from the cohesive zone model should match that of the stationary crack prior to crack initiation. However, due to the softening introduced by the cohesive elements, the curves obtained from the cohesive zone models deviate from the

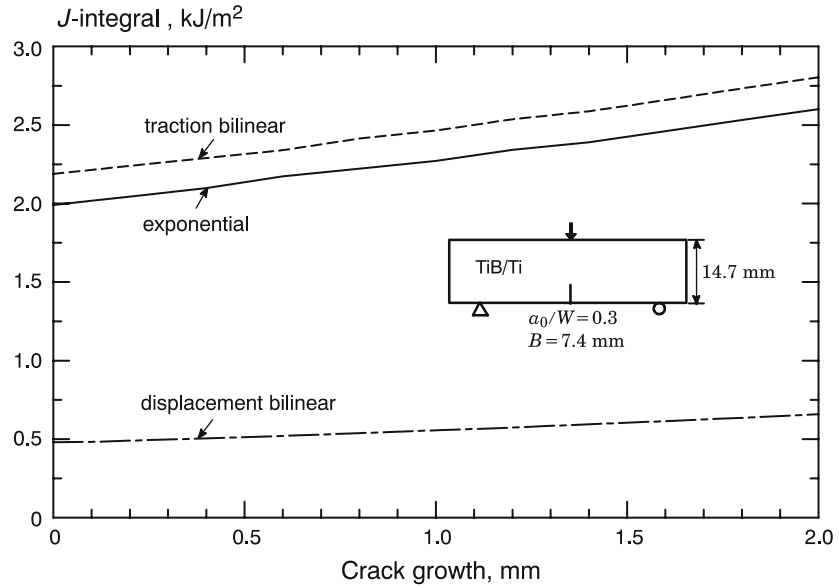

Figure 9. J-integral versus crack growth responses (J_R curves) obtained from the three cohesive zone models for the TiB/Ti SE(B) specimen ($p = 0.84$).

stationary crack curve. Such difference is more pronounced for the exponential and the traction-based bilinear models, which assume that the metal phase controls the crack growth. The curve obtained from the displacement-based bilinear model closely follows the stationary crack curve in the initial stage of loading, but starts to show a difference as it approaches crack initiation. The J-integral value calculated from the stationary crack model at crack initiation load is $0.28\,\mathrm{kJ/m^2}$. As shown in Figure 11, J_{init} obtained from the displacement-based bilinear model shows a relatively small difference with that of the stationary crack model compared to the difference shown by the other two models (78% versus 600%). Note that the J_{init} for the stationary crack model and the intrinsic cohesive zone model do not match, unless another model is employed, e.g. extrinsic cohesive zone model (Celes et al., 2005). Figure 11 indicates that the exponential and the traction-based bilinear models overestimate the actual J value at a given load. Note that for FGMs, the J-integral does not correspond to the cohesive energy density at specific locations of the current crack front. Instead, it represents effects of the cohesive energy density over the whole cohesive zone and the background material gradation (Jin and Dodds, 2004). This explains why the J_{init} values shown in Figure 11 are higher than the $\Gamma^{c}_{\mathrm{eff}}$ values shown in Figure 6.

Figures 10 and 11 show that the assumption of metal phase controlling the crack growth, i.e. critical displacement of the metal phase controlling the cohesive element extinction, is inappropriate for the TiB/Ti FGM considered in the present study. On the other hand, results obtained from the displacement-based bilinear model seem to be more reasonable and closely capture the fracture and crack growth behaviors of the TiB/Ti FGM.

We now adopt the displacement-based bilinear cohesive model to investigate the effect of material gradient on the J_R curve for the TiB/Ti FGM SE(B) specimen.

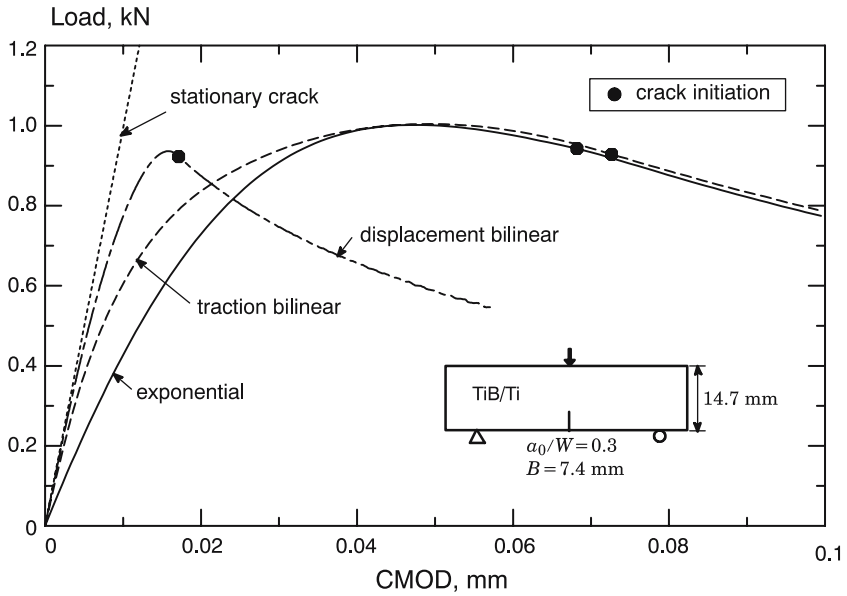

Figure 10. Load versus CMOD responses obtained from the three cohesive zone models and the stationary crack model for the TiB/Ti SE(B) specimen ($p = 0.84$).

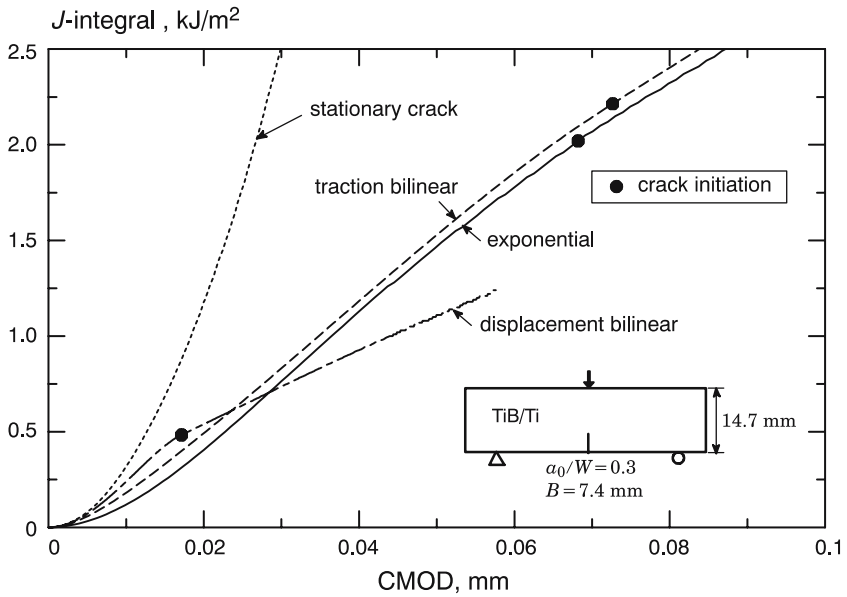

Figure 11. *J*-integral versus CMOD responses obtained from the three cohesive zone models and the stationary crack model for the TiB/Ti SE(B) specimen ($p = 0.84$).

Figure 12 shows the J_R curves for various values of p in Equation (20). The "built-in" toughening behavior of the FGM, i.e. increase of J-integral with crack growth, is shown for all cases. J-integral at fixed crack growth increases with decreasing p – a smaller p corresponds to a higher metal volume fraction, which leads to a higher cohesive traction and energy for the FGM, thereby enhancing the crack growth resistance.

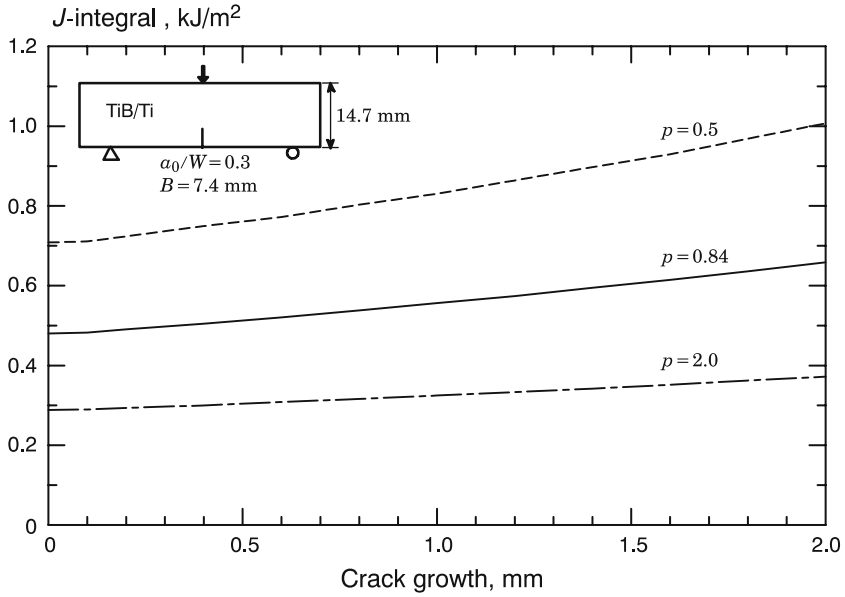

Figure 12. J-integral versus crack growth responses (J_R curves) for the TiB/Ti SE(B) specimen obtained from the displacement-based bilinear cohesive zone for different values of exponent p.

Figure 13 shows the J_R curve for the SE(T) specimen in comparison to that for the SE(B) specimen, where $p=0.84$ for both specimens. The J_R curve for the SE(T) specimen is slightly (5%) higher than that for the SE(B) specimen. Linear elastic analyses performed for the SE(B) and SE(T) specimens show that both specimens have negative T-stresses and the biaxiality ratios $\beta(=T\sqrt{a}/K_I)$ are -0.14 and -0.51, respectively. These results indicate that the specimen configuration (or T-stress) has insignificant effect on the J_R curve for the TiB/Ti FGM considered in the present study, i.e. where crack growth remains in the relatively brittle region of the FGM.

5. Application of cohesive zone model to modified boundary layer model

5.1. Modified boundary layer model for FGMs

The MBL formulation has been adopted by many researchers to analyze the elastic–plastic crack-tip fields in homogeneous materials (e.g., Larsson and Carlsson, 1973; Bilby et al., 1986; Betegon and Hancock, 1991; Xia and Shih, 1995). Recently, Shim et al. (2006a) proposed a MBL model for FGMs with material gradient parallel to the crack plane. In their work, they selected the middle-crack tension, M(T), specimen as the reference configuration for the MBL model. Figure 14 shows the geometry of the MBL model. The material is graded parallel to the crack plane and material properties are symmetric with respect to the centerline of the model. The symmetric loading conditions and material properties enable the use of a quarter model. Considering the quarter model (shaded region in Figure 14), tractions are applied to the top edge of the model and also to the lateral edge of the model. Now, the key task becomes the determination of the corresponding traction boundary conditions that generate the desired K–T field near the crack-tip. Figure 15 shows the

procedure to obtain the traction boundary conditions. Only the linear-elastic material properties are considered for this procedure. First, a unit traction $\sigma_{\text{top}}^{\text{unit}}$ is applied to the top edge of the model, Figure 15(a). This unit traction produces $K_{I,\text{top}}^{\text{unit}}$ and $T_{\text{top}}^{\text{unit}}$ at the crack-tip. As a second step, a unit traction $\sigma_{\text{lateral}}^{\text{unit}}$ is applied to lateral edge of the model, Figure 15(b). Similarly, this unit traction produces $K_{I,\text{lateral}}^{\text{unit}}$ and $T_{\text{lateral}}^{\text{unit}}$ at the crack-tip. For homogeneous materials, $K_{I,\text{lateral}}^{\text{unit}} = 0$ since the stress parallel to the crack plane does not contribute to the mode I SIF. However, for graded nonhomogeneous materials, stress parallel to the crack plane contributes to the mode I SIF thru secondary bending (Shim et al., 2006a). The SIF and T-stress values are proportional to the applied tractions. Let K_I and T denote the desired values of mode I SIF and the T-stress. Then these two values can be expressed by

$$K_I = fK_{I,\text{top}}^{\text{unit}} + gK_{I,\text{lateral}}^{\text{unit}}, \tag{21}$$

$$T = fT_{\text{top}}^{\text{unit}} + gT_{\text{lateral}}^{\text{unit}}, \tag{22}$$

where

$$f = \frac{\sigma_{\text{top}}}{\sigma_{\text{top}}^{\text{unit}}}, \qquad g = \frac{\sigma_{\text{lateral}}}{\sigma_{\text{lateral}}^{\text{unit}}}, \tag{23}$$

where σ_{top} and σ_{lateral} are the traction boundary conditions needed to obtain K_I and T. By using Equations (21)–(23), the traction boundary conditions for the MBL model can be easily determined for any desired K_I and T, Figure 15(c).

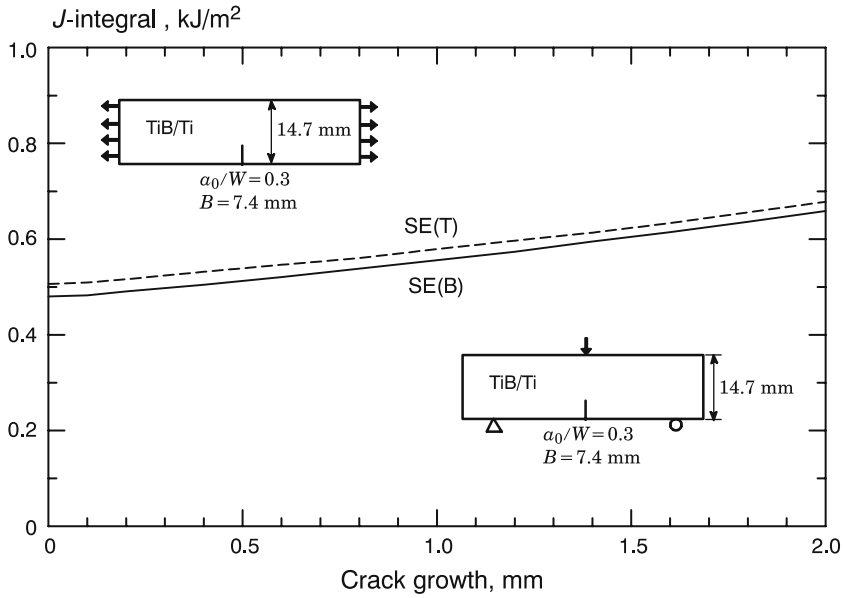

Figure 13. J-integral versus crack growth responses (J_R curves) obtained from the displacement-based bilinear cohesive zone model for TiB/Ti SE(T) and SE(B) specimens ($p = 0.84$).

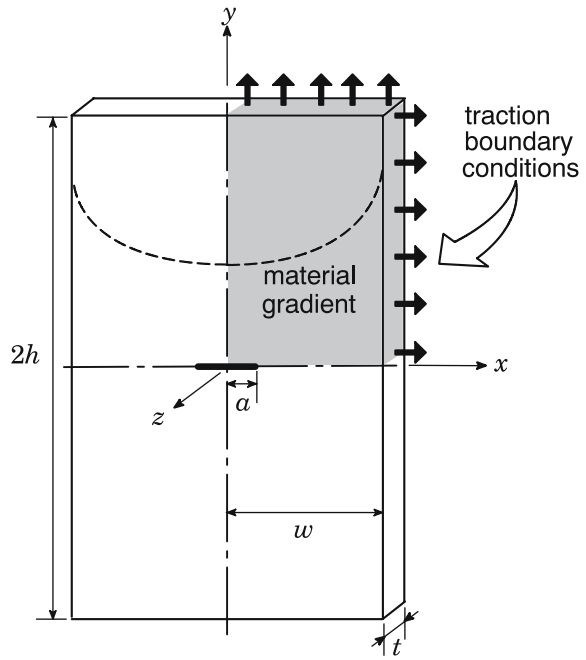

Figure 14. Schematics of the MBL model. Material properties are graded in the x-direction and symmetric with respect to the centerline of the model. The traction boundary conditions are applied to the top and lateral edges of the model.

5.2. Crack growth in FGM using cohesive zone and MBL models

This subsection describes the application of cohesive zone and MBL models to analyze crack growth resistance in TiB/Ti FGM. In the present study, we employ the MBL model of Shim et al. (2006a). In this context, the SE(B) and SE(T) specimens, described in Section 4, represent the arbitrary geometry conditions which are simulated via the MBL model. Figure 16 depicts the set-up of the MBL model for crack growth analysis. The material gradient of the MBL model is expressed in terms of volume fraction of Ti. Since the volume fraction of Ti must be between zero and one, the material properties are graded only in the region corresponding to the specimen. The other regions of the MBL model have either homogeneous material properties of Ti ($V_{Ti} = 1$) or TiB($V_{Ti} = 0$) as shown in Figure 16. The interface-cohesive elements are placed only over the initial uncracked ligament of the MBL model.

Figure 17 shows the procedure adopted in the present study to perform elastic–plastic crack growth analysis using the MBL model. First, we perform elastic analysis for the specimen (stationary crack model without cohesive elements), considering only the elastic material properties (E and ν). The elastic analysis yields K_I and T (calculated from interaction integral technique implemented in WARP3D – see Walters et al., 2005, 2006),which are used to determine the traction boundary conditions for the MBL model. The traction boundary conditions are determined from the elastic analysis of the MBL model (stationary crack model without cohesive elements) only considering E and ν (see Figure 15). The determined traction boundary conditions are applied to the MBL model, which has interface-cohesive elements, for

crack growth analysis. The elastic and plastic material properties (E, ν, σ_{YS}, and n) are considered for the crack growth analysis. The crack growth resistance behavior, i.e. the J_R curve, is obtained from the MBL model. This result is compared with that obtained from the crack growth analysis of the specimen, i.e. the arbitrary geometry, to validate the applicability of the MBL model to crack growth analysis.

The FE mesh employed for the MBL model is similar to the one used for the SE(B) and SE(T) specimens (see Figure 5). The mesh has two layers of elements in the thickness direction and all nodes in the model are constrained in the thickness direction to obtain plane–strain conditions. The FE model has 5,040 nodes and 3,154 elements. The size of the MBL model must be determined so that the K–T dominant region of the specimen is embedded within that of the MBL model (Shim et al., 2006a,b). In the present study, the half-width w (Figure 14) of the MBL model is set to 200 mm and the height $h = 2w$.

5.3. Comparison of J resistance curves

The three cohesive zone models described in Section 2 are adopted for the MBL model for comparison. Figure 18 compares the J_R curves obtained from the SE(B) specimen with those obtained from the MBL model. The J_R curves obtained from the MBL model using exponential and traction-based bilinear cohesive zone models are approximately 100% higher than those from the SE(B) specimen. Such difference arise from the fact that the traction boundary conditions (determined from the elastic analysis of a stationary crack) fail to produce the desired K–T stress field when applied to the MBL model with interface-cohesive elements. This can be inferred from Figure 11, where the J-integral values obtained from the exponential and traction based bilinear models show large difference with that from the stationary crack model prior to crack growth.

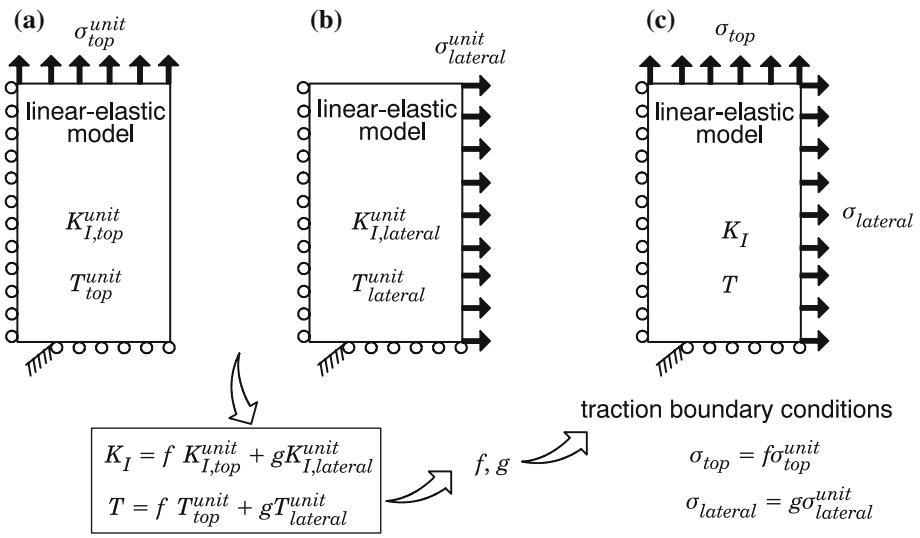

Figure 15. Procedure to obtain the traction boundary conditions for the MBL model. Unit traction applied to (a) the top edge and (b) the lateral edge of the model. Equations (21)–(23) yield the traction boundary conditions required to generate K_I and T at the crack-tip (c).

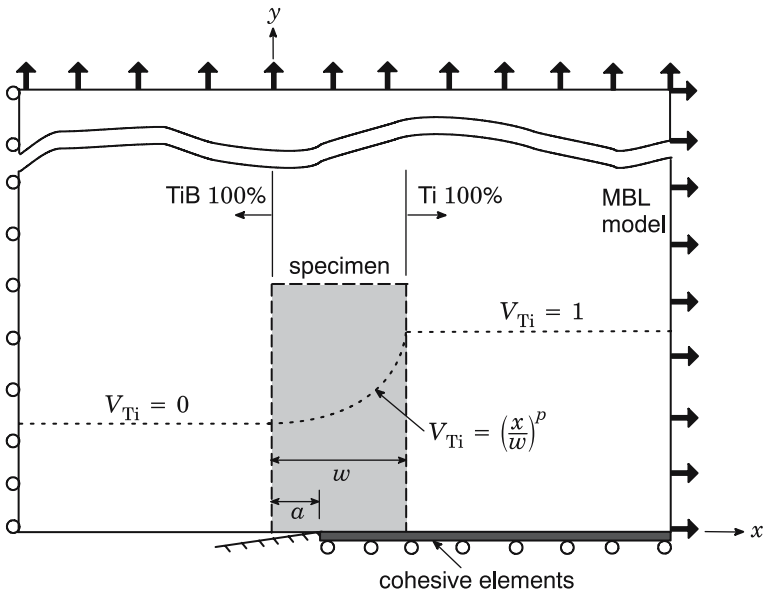

Figure 16. Setup of MBL model for crack growth analysis for TiB/Ti FGM. Material properties are graded only in the region corresponding to the specimen.

In contrast, as shown in Figure 18, the J_R curves obtained from the MBL model and the SE(B) specimen using the displacement-based bilinear model show good agreement, which demonstrate that the traction boundary conditions obtained from the stationary crack correspondingly produce the desired K–T stress field for the MBL model with interface-cohesive elements. Figure 19 compares the J_R curves obtained from the MBL model and the SE(T) specimen, both using the displacement-based bilinear model, which show good agreement.

The exponential and the traction-based bilinear model not only overestimate the J-integral values (Figures 9 and 11), but also fail to produce the desired K–T stress field for the MBL model. On the other hand, the displacement-based bilinear model closely calculates the actual J-integral values, and thus serves as a suitable cohesive zone model for the MBL model.

6. Concluding remarks

In this study, the J resistance behavior of TiB/Ti FGM is investigated by employing a phenomenological cohesive zone model (coupled with experimental calibrations) and a MBL model. The present study only considers mode I, plane–strain conditions. Two existing models and a new cohesive zone model for FGMs are adopted to simulate the crack growth resistance. The two existing models, i.e. exponential and traction-based bilinear models, assume that the metal phase (Ti) controls the crack growth and thus uses the critical displacement of the metal phase as the element extinction criterion. Such criterion may be applicable for conventional composites, which have distinct matrix and inclusion phases and uniform microstructures. However, FGMs have a complex interconnecting region with graded microstructures that dominate the response. The cohesive zone model proposed in

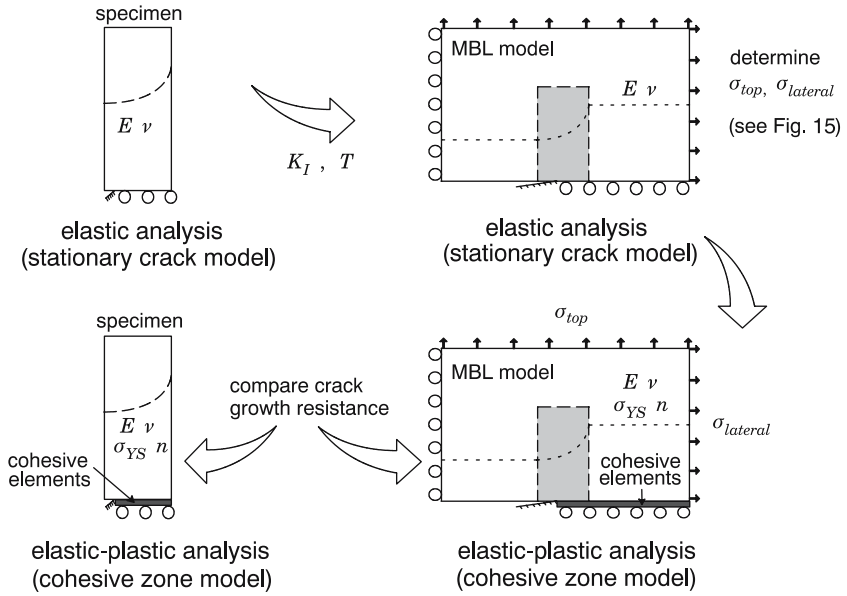

Figure 17. Procedure adopted in the present study to perform elastic–plastic crack growth analysis using the MBL model.

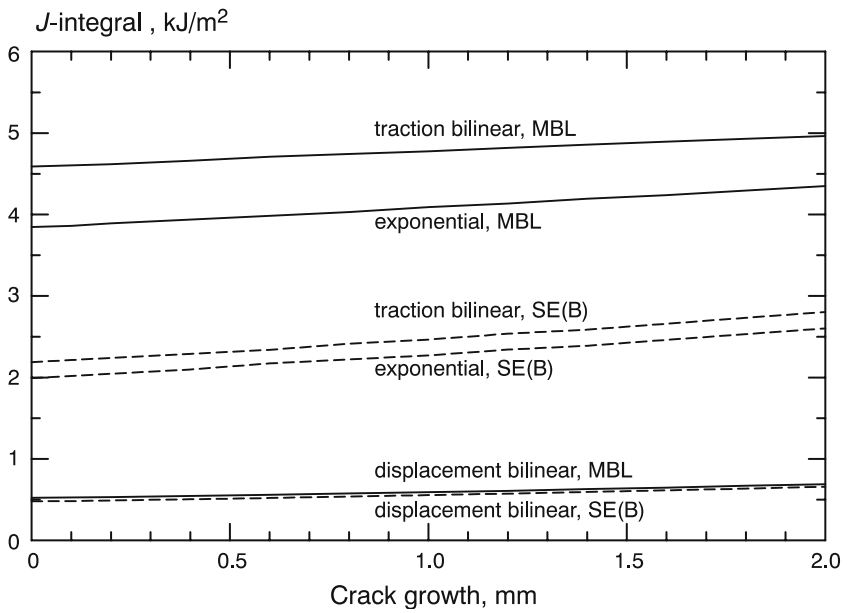

Figure 18. Comparison of J-integral versus crack growth responses (J_R curves) obtained from the MBL model and SE(B) specimen ($p = 0.84$).

the present study, i.e. displacement-based bilinear model, adopts a volume fraction-based element extinction criterion, which more effectively reflects the effects of graded microstructure.

The three cohesive zone models are employed to simulate the crack growth resistance of a TiB/Ti SE(B) specimen. The cohesive parameters are calibrated by

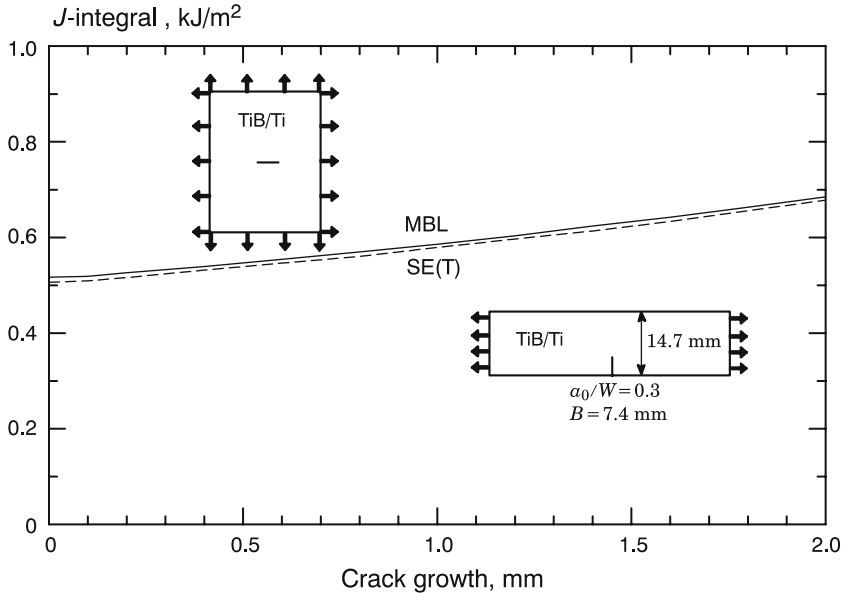

Figure 19. Comparison of J-integral versus crack growth responses (J_R curves) obtained from the MBL model and SE(T) specimen ($p = 0.84$) using displacement-based bilinear cohesive zone model.

matching the numerical results to the crack initiation load obtained from the experiment. Although the load versus crack growth responses obtained from the three cohesive zone models show similar results, the J_R curves show a large difference. Numerical results of the present study demonstrate that the J values obtained from the exponential and traction-based bilinear cohesive zone models overestimate the actual J value. On the other hand, the displacement-based bilinear cohesive zone model yields more reasonable results and closely captures the fracture and crack growth behaviors of TiB/Ti FGM.

The effect of specimen configuration, i.e. T-stress, on the J_R curve is insignificant for the TiB/Ti FGM considered in the present study. This is due to the fact that the crack growth remains within the relatively brittle region of the FGM. The effect of T-stress on the J_R curve may be more significant for regions with relatively high ductility. This issue is not addressed in the present study since it is not within the primary scope of the work. However, the present numerical results suggest that the displacement-based bilinear model can be employed to simulate crack growth in TiB/Ti FGMs when the crack-tip remains within the relatively brittle region, where V_{Ti} is less than 0.7.

The applicability of the cohesive zone model to the MBL model is investigated in the present study. The exponential and traction-based bilinear cohesive zone models fail to yield the desired K–T stress field. The J_R curves obtained from the MBL model using these two cohesive zone models show approximately 100% difference to that obtained from the SE(B) specimen. On the other hand, the displacement-based bilinear model yields the desired K–T stress field for the MBL model, and thus yields J_R curves that match the ones obtained from the SE(B) and SE(T) specimens. These results verify that the proposed displacement-based bilinear model serves as a suitable cohesive zone model for the MBL model.

The crack growth resistance of a FGM now can be investigated by using the MBL model in conjunction with the cohesive zone model. This approach will serve as a powerful and useful tool for investigating the fracture and crack growth behaviors of ceramic/metal FGMs. However, as failure process in ceramic/metal FGMs become better understood, e.g. through more experiments, the FGM cohesive zone model proposed in the present study may be revisited accordingly.

Acknowledgements

This work was supported by the M.T. Geoffery Yeh Endowed Chair Fund at the University of Illinois, Urbana-Champaign.

References

Abanto-Bueno, J. and Lambros, J. (2002). Investigation of crack growth in functionally graded materials using digital image correlation. *Engineering Fracture Mechanics* **69**, 1695–1711.

Anlas, G., Santare, M.H. and Lambros, J. (2000). Numerical calculation of stress intensity factors in functionally graded materials. *International Journal of Fracture* **104**, 131–143.

Baylor, J. (1998). A numerical simulation of impact-induced damage of composite materials. Master Thesis, University of Illinois at Urbana-Champaign.

Betegon, C. and Hancock, J.W. (1991). Two-parameter characterization of elastic-plastic crack-tip fields. *ASME Journal of Applied Mechanics* **58**, 104–110.

Bilby, B.A., Cardew, G.E., Goldthorpe, M.R. and Howard, I.C. (1986). A finite element investigation of the effect of specimen geometry on the fields of stress and strain at the tip of stationary cracks. *Size Effect in Fracture*. Institute of Mechanical Engineers, 37–46.

Camacho, G.T. and Ortiz, M. (1996). Computational modeling of impact damage in brittle materials. *International Journal of Solids and Structures* **33**, 2899–2938.

Carpenter, R.D., Liang, W.W., Paulino, G.H., Gibeling, J.C. and Munir, Z.A. (1999). Fracture testing and analysis of a layered functionally graded Ti/TiB beam in 3-point bending. *Materials Science Forum* **308–311**, 837–842.

Celes,W., Paulino, G.H. and Espinha, R. (2005). A compact adjacency-based topological data structure for finite element mesh representation. *International Journal for Numerical Methods in Engineering* **64**, 1529–1556.

Eischen, J.W. (1987). Fracture of non-homogeneous materials. *International Journal of Fracture* **34**, 3–22.

Erdogan, F. (1995). Fracture mechanics of functionally graded materials. *Composites Engineering* **5**, 753–770.

Geubelle, P.H. and Baylor, J. (1998). Impact-induced delamination of laminated composites: a2D simulation. *Composites Part B Engineering* **29**, 589–602.

Giannakopoulos, A.E., Suresh, S., Finot, M. and Olsson, M. (1995). Elastoplastic analysis of thermal cycling: layered materials with compositional gradients. *Acta Metallurgica et Materialia* **43**, 1335–1354.

Gu, P. and Asaro, R.J. (1997). Crack deflection in functionally graded materials. *International Journal of Solids and Structures* **34**, 3085–3098.

Gullerud, A.S., Koppenhoefer, K.C., Roy, Y.A., RoyChowdhury, S., Walters, M., Bichon, B., Cochran, K. and Dodds Jr., R.H. (2004). *WARP3D Release 15 Manual*, Civil Engineering, Report No. UIUC-ENG-95-2012, University of Illinois at Urbana-Champaign.

Jin, Z.-H., Paulino, G.H. and Dodds Jr., R.H. (2002). Finite element investigation of quasi-static crack growth in functionally graded materials using a novel cohesive zone fracture model. *ASME Journal of Applied Mechanics* **69**, 370–379.

Jin, Z.-H., Paulino, G.H. and Dodds Jr., R.H. (2003). Cohesive fracture modeling of elastic-plastic crack growth in functionally graded materials. *Engineering Fracture Mechanics* **70**, 1885–1912.

Jin, Z.-H. and Dodds Jr., R.H. (2004). Crack growth resistance behavior of a functionally graded material: computational studies. *Engineering Fracture Mechanics* **71**, 1651–1672.

Kandula, S.S.V., Abanto-Bueno, J., Geubelle, P.H. and Lambros, J. (2005). Cohesive modeling of dynamic fracture in functionally graded materials. *International Journal of Fracture* **132**, 275–296.

Kim, J.-H. and Paulino, G.H. (2002a). Finite element evaluation of mixed-mode stress intensity factors in functionally graded materials. *International Journal for Numerical Methods in Engineering* **53**, 1903–1935.

Kim, J.-H. and Paulino, G.H. (2002b). Isoparametric graded finite elements for nonhomogeneous isotropic and orthotropic materials. *ASME Journal of Applied Mechanics* **69**, 502–514.

Kim, J.-H. and Paulino, G.H. (2003). *T*-stress, mixed-mode stress intensity factors, and crack initiation angles in functionally graded materials: a unified approach using the interaction integral method. *Computer Methods in Applied Mechanics and Engineering* **192**, 1463–1494.

Kim, J.-H. and Paulino, G.H. (2004). Simulation of crack propagation in functionally graded materials under mixed-mode and non-proportional loading. *International Journal of Mechanics and Materials in Design* **1**, 63–94.

Klein, P.A., Foulk, J.W., Chen, E.P., Wimmer, S.A. and Gao, H. (2000). Physics-based modeling of brittle fracture: cohesive formulations and the application of meshfree methods. Sandia National Laboratory, Technical Report, SAND2001–8099.

Larsson, S.G. and Carlsson, A.J. (1973). Influence of non-singular stress terms and specimen geometry on small-scale yielding at crack tips in elastic-plastic materials. *Journal of the Mechanics and Physics of Solids* **21**, 263–277.

Li, H., Lambros, J., Cheeseman, B.A. and Santare, M.H. (2000). Experimental investigation of the quasi-static fracture of functionally graded materials. *International Journal of Solids and Structures* **37**, 3715–3732.

Moon, R.J., Hoffman, M., Hilden, J., Bowman, K.J., Trumble, K.P. and Rodel, J. (2002). *R*-curve behavior in alumina-zirconia composites with repeating graded layers. *Engineering Fracture Mechanics* **69**, 1647–1665.

Needleman, A. (1987). A continuum model for void nucleation by inclusion debonding. *ASME Journal of Applied Mechanics* **54**, 525–531.

Needleman, A. (1990). An analysis of tensile decohesion along an interface. *Journal of the Mechanics and Physics of Solids* **38**, 289–324.

Nelson, G. and Ezis, A. (1996). Functionally graded material (FGM) armor in the TiB/Ti system (U). CERCOM Report.

Ortiz, M. and Pandolfi, A. (1999). Finite-deformation irreversible cohesive elements for three-dimensional crack propagation analysis. *International Journal for Numerical Methods in Engineering* **44**, 1267–1282.

Paulino, G.H., Carpenter, R.D., Liang, W.W., Munir, Z.A. and Gibeling, J.C. (2001). Fracture testing and finite element modeling of pure Titanium. *Engineering Fracture Mechanics* **68**, 1417–1432.

Rangaraj, S. and Kokini, K. (2004). A study of thermal fracture in functionally graded thermal barrier coatings using a cohesive zone model. *ASME Journal of Engineering Materials and Technology* **126**, 103–115.

Roy, Y.A. and Dodds Jr., R.H. (2001). Simulation of ductile crack growth in thin aluminum panels using 3-D surface cohesive elements. *International Journal of Fracture* **110**, 21–45.

Shim, D.-J., Paulino, G.H. and Dodds Jr., R.H. (2006a). A boundary layer framework considering material gradation effects. *Engineering Fracture Mechanics* **73**, 593–615.

Shim, D.-J., Paulino, G.H. and Dodds Jr., R.H. (2006b). Effect of material gradation on *K*-dominance of fracture specimens. *Engineering Fracture Mechanics* **73**, 643–648.

Siegmund, T. and Needleman, A. (1997). Numerical simulation of fast crack growth in brittle solids. *Journal of the Mechanics and Physics of Solids* **42**, 1397–1434.

Tamura, I., Tomota,Y. and Ozawa, H. (1973). Strength and ductility of Fe-Ni-C alloys composed of austenite and martensite with various strength. *Proceedings of the Third International Conference on Strength of Metals and Alloys*, vol. 1, Cambridge: Institute of Metals, 611–615.

Tohgo, K., Suzuki, T. and Araki, H. (2005). Evaluation of *R*-curve behavior of ceramic-metal functionally graded materials by stable crack growth. *Engineering Fracture Mechanics* **72**, 2359–2372.

Tvergaard, V. (1990). Effect of fiber debonding in a whisker-reinforced metal. *Materials Science and Engineering* A **125**, 203–213.

Tvergaard, V. (2001). Crack growth predictions by a cohesive zone model for ductile fracture. *Journal of the Mechanics and Physics of Solids* **49**, 2191–2207.

Tvergaard,V. (2002). Theoretical investigation of the effect of plasticity on crack growth along a functionally graded region between dissimilar elastic-plastic solids. *Engineering Fracture Mechanics* **69**, 1635–1645.

Tvergaard, V. and Hutchinson, J.W. (1992). The relation between crack growth resistance and fracture process parameters in elastic-plastic solids. *Journal of the Mechanics and Physics of Solid* **40**, 1377–1397.

Walters, M.C., Paulino, G.H. and Dodds Jr., R.H. (2004). Stress intensity factors for surface cracks in functionally graded materials under mode I thermomechanical loading. *International Journal of Solids and Structures* **41**, 1081–1118.

Walters, M.C., Paulino, G.H. and Dodds Jr., R.H. (2005). Interaction-integral procedures for 3-D curved cracks including surface tractions. *Engineering Fracture Mechanics* **72**, 1635–1663.

Walters, M.C., Paulino, G.H. and Dodds Jr., R.H. (2006). Computation of mixed-mode stress intensity factors for cracks in three-dimensional functionally-graded solids. *ASCE Journal of Engineering Mechanics* **132**, 1–15.

Williamson, R.L., Rabin, B.H. and Drake, J.T. (1993). Finite element analysis of thermal residual stresses at graded ceramic-metal interfaces, part I: model description and geometrical effects. *Journal of Applied Physics* **74**, 1310–1320.

Xia, L. and Shih, C.F. (1995). Ductile crack growth – I. A Numerical study using computational cells with microstructurally-based length scales. *Journal of the Mechanics and Physics of Solids* **43**, 233–259.

Xu, X. and Needleman, A. (1996). Numerical simulations of dynamic crack growth along an interface. *International Journal of Fracture* **74**, 289–324.

Zavattieri, P. and Espinosa, H. (2001). Grain level model analysis of crack initiation and propagation in brittle materials. *Acta Materialia* **49**, 4291–4311.

Zhang, Z. (2003). Cohesive zone modeling of dynamic failure in homogeneous and functionally graded materials. Master Thesis, University of Illinois at Urbana-Champaign.

Zhang, Z. and Paulino, G.H. (2005). Cohesive zonemodeling of dynamic failure in homogenous and functionally graded materials. *International Journal of Plasticity* **21**, 1195–1254.